ACS Catalysis

Review

pubs.acs.org/acscatalysis

Recent Insights into Manganese Oxides in Catalyzing Oxygen Reduction Kinetics

Kelsey A. Stoerzinger,*[,†] Marcel Risch,[‡] Binghong Han,[†] and Yang Shao-Horn*[,†,‡,§]

[†]Department of Materials Science & Engineering, [‡]Research Laboratory of Electronics, [§]Department of Mechanical Engineering, Massachusetts Institute of Technology, Cambridge, Massachusetts 02139, United States

ABSTRACT: The sluggish kinetics of the oxygen reduction reaction (ORR) limit the efficiency of numerous oxygen-based energy conversion devices such as fuel cells and metal-air batteries. Among earth abundant catalysts, manganese-based oxides have the highest activities approaching that of precious metals. In this Review, we summarize and analyze literature findings to highlight key parameters that influence the catalysis of the ORR on manganese-based oxides, including the number of electrons transferred as well as specific and mass activities. These insights can help develop design guides for highly active ORR catalysts and shape future fundamental research to gain new knowledge regarding the molecular mechanism of ORR catalysis.

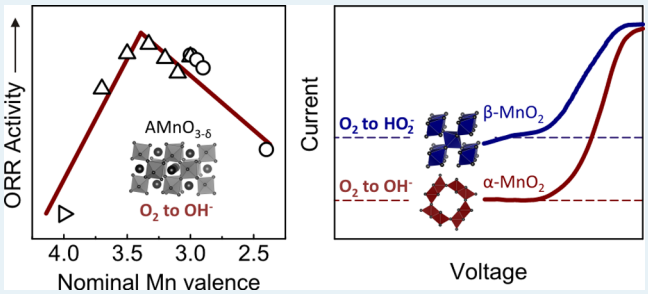

KEYWORDS: *manganese oxide, electrocatalysis, oxygen reduction reaction, alkaline, valence, peroxide disproportionation*

1. INTRODUCTION

Efficient catalysis of the oxygen reduction reaction (ORR) is critical to electrochemical energy conversion, as the dominant source of loss in fuel cells[1] and discharge of metal-air batteries.[2−5] Platinum and its alloys have been extensively investigated due to their high activity for the ORR[1,6] and are utilized commercially in proton exchange membrane fuel cells operated near room temperature for electric vehicle applications. However, material cost and scarcity have limited scaling-up of Pt-based catalysts for renewable energy applications, and have motivated the study of alternative, more abundant catalysts.[7−10] Moving from acidic to basic solution, earth abundant metal oxides exhibit ORR activities that can approach those of Pt−metal.[11,12]

Catalysts with particular promise to catalyze the ORR in basic solution fall within the family of manganese oxides, which are abundant, inexpensive, and nontoxic with rich oxide chemistry. Some manganese oxides are among the most active oxide catalysts.[11,12] We show that the activities per material cost for Pt/C and $LaMnO_{3+\delta}$ can be comparable while α-MnO_2 can have higher activity per cost than Pt/C, where the cost was approximated on a metals basis (weighted elemental contribution from La and/or Mn, Figure 1).

Here, we will compare the specific activity being current per oxide surface (mA/cm^2_{oxide}) and the mass activity being current per oxide mass (A/g_{oxide}) for Mn-based oxides. The specific activity is a practical approximation of the activity per active site (or turnover frequency), which is often unknown, and reflects the intrinsic activity of chemistry. High mass activity—determined by particle size and morphology—is important for the development of catalysts for practical devices, which reduces the cost, size, and weight. The optimal electrocatalyst should have both high specific activity and high mass activity. In addition to consideration of ORR current, four-electron reduction of molecular oxygen is desirable. The ORR in alkaline media can proceed by a four-electron reduction pathway to produce hydroxide (OH^-) or by a two-electron reduction pathway to produce hydroperoxide (HO_2^-).[16] The ORR proceeds by the four-electron pathway on Pt-based catalysts that can dissociate the oxygen−oxygen bond.[17,18] Many active oxides for the ORR exhibit a number of electrons transferred close to four,[14,19−21] which can be influenced by factors such as the valence state[22] of metal ions and the type of metal ions.

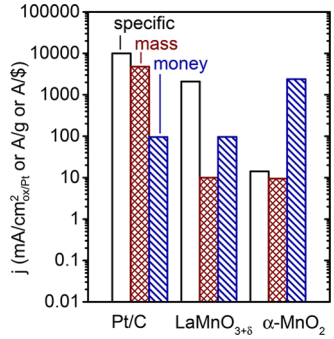

Figure 1. Specific ($mA/cm^2_{ox/Pt}$; white bars), mass (A/g; red crossed bars), and monetary (A/$; market price of metals Pt, Mn, and La;[13] hatched blue bars) of Pt/C,[14] $LaMnO_{3+\delta}$,[11] and α-MnO_2,[15] at 0.8 V vs RHE in 0.1 M KOH.

Received: July 10, 2015
Revised: August 30, 2015
Published: September 1, 2015

DOI: 10.1021/acscatal.5b01444
ACS Catal. 2015, 5, 6021−6031

In this review, we focus on the recent development of manganese oxide catalysts for the ORR in alkaline media. First, we introduce the electrochemical techniques for the ORR process, comparing the benefits and shortcomings of different electrode geometries and measurement techniques. We next assess the importance of the Mn valence state in catalysis of the ORR. Manganese oxides—both simple (containing only Mn and O) and complex (where the valence can be tuned by the addition of other cations in the spinel or perovskite structure)—have been synthesized from diverse techniques ranging from electodeposition of amorphous materials to epitaxial deposition of crystalline films. Comparing specific activities enables a true understanding of the role of Mn valence in catalysis. While computations of the reaction mechanism are not extensive, experiments show the numerous polymorphs for even the "simple" MnO_2 can catalyze the ORR to produce hydroperoxide or hydroxide, and combinations thereof. We therefore consider the role of Mn valence in determining the products of ORR catalysis, as well as the relation between the activity toward peroxide disproportionation and reduction and the apparent reaction mechanism. In situ evaluation of catalysts highlights the reduction of Mn under ORR conditions, as well as the potential and pH dependence of material stability, also considered through computation. These cumulative studies have developed great insight into the mechanism of oxygen reduction to hydroperoxide and hydroxide, as well as support interactions.

2. MEASURING AND QUANTIFYING ORR KINETICS: SPECIFIC AND MASS ACTIVITIES AND THE NUMBER OF ELECTRONS TRANSFERRED

In order to measure the ORR activity of a catalyst, three methods are commonly employed. We discuss their strengths and weaknesses; in particular, not all methods yield reliable measurements of the mass and specific activity. For a detailed comparison of different estimations of catalyst surface area, we refer the reader to the IUPAC recommendation[23] and our previous review.[24] First, catalysts can be included in gas diffusion electrodes[25] (GDEs) or fuel cell membrane electrode assemblies (MEAs) in a two-electrode setup, which can be tested in alkaline fuel cells or metal-air batteries.[1,26] These GDEs and MEAs have thicknesses on the order of tens to hundreds of microns and typically consist of carbon and binder in addition to the catalyst. It is challenging in GDEs or MEAs to assess activity, and especially specific activity, due to the ill-defined electrochemically active (exposed to the electrolyte and electrically contacted) catalyst surface area and oxygen transport losses in the thick composite, which are difficult to separate from ORR kinetics. Nonetheless, these tests are needed to demonstrate the usefulness of electrocatalysts in actual devices.

Second, rotating disk electrode (RDE) measurements, with well-defined oxygen transport by convection, can remove the influence of oxygen transport on ORR kinetics.[27] In this measurement, oxide powder is often dispersed with a high surface area carbon and binder such as ion-exchanged Nafion[14] to form a composite layer of ideally less than 100 nm to approximate a flat surface.[28] Using the RDE method, the apparent number of electrons transferred can be deduced via the relation between limiting current (normalized to the projected area of the disk) and rotation speed, analyzed with the Levich equation.[29] This analysis is only applicable if a sufficient amount of catalyst is added to be able to reach the limiting current within 10% of its theoretical value[28] (dashed lines in Figure 2). The expected ORR limiting current densities

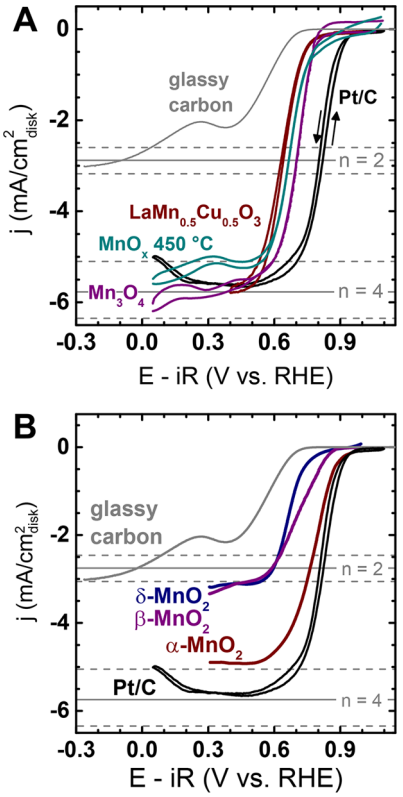

Figure 2. Geometric current density (normalized to disk area) of (A) $LaMn_{0.5}Cu_{0.5}O_3$,[14] Mn_3O_4,[12] and electrodeposited MnO_x[33] (after annealing at 450 °C) and (B) δ-MnO_2,[15] β-MnO_2,[15] and α-MnO_2.[15] Both panels contain Pt supported on carbon (Pt/C; 46 wt % TKK, Japan)[14] and glassy carbon as references. All measurements were obtained by cyclic voltammetry at 1600 rpm. Theoretical limiting currents for the four-electron and two-electron pathways are indicated by solid lines together with a ±10% margin (dashed lines). Reproduced from refs 14 and 33 with permission from the Electrochemical Society, copyright 2010 and 2013, and refs 15 and 12 with permission from the American Chemical Society, copyright 2014 and 2012.

are close to 5.8 mA/cm_{disk}^2 at 1600 rpm in 0.1 M KOH at room temperature[30,31] for the hydroxide pathway (four electrons transferred; $n = 4$), as shown for Pt/C, $LaMn_{0.5}Cu_{0.5}O_3$, and Mn_3O_4 in Figure 2A, and half that (2.9 mA/cm^2_{disk}) for the hydroperoxide pathway (two electrons transferred; $n = 2$) as shown for glassy carbon in Figure 2A. The number of electrons transferred or the amount of peroxide generated during the ORR can be also obtained with rotating ring disk electrode (RRDE) measurements, where the disk is surrounded by a Pt ring polarized such that oxidation of any HO_2^- from the ORR is diffusion limited.[32] Taking the ratio of the ring current to the total measured current, normalized by the calibrated collection efficiency, enables estimation of the fraction of peroxide produced. This allows deconvolution of a mixed pathway, however only HO_2^- that escapes from the electrode will be detected, and side reactions (e.g., Mn reduction) must not occur. In summary, the (R)RDE method can yield quantitative results for specific activity (if surface area is known), mass activity, and the number of electrons transferred (or the product ratio of hydroxide to hydroperoxide).

DOI: 10.1021/acscatal.5b01444
ACS Catal. 2015, 5, 6021−6031

Third, quiescent electrodes can be measured in the kinetic limited regime near the onset of catalytic activity in a three-electrode geometry using cyclic voltammetry or potentiostatic measurements. Kinetically controlled currents can be confirmed by assuring the measured activity does not change with increased oxygen flow or electrolyte circulation.[34] This method is particularly useful to study ORR kinetics on films deposited on metal or semiconducting (transparent) oxide substrates in the absence of rotation, as it is typically not straightforward to incorporate these samples in the RDE setup.[35] Examining ORR kinetics on oxide thin films allows a more accurate measure of the specific activity of solely the oxide surface[34,36] in comparison to ORR studies of composite electrodes that consist of oxide and carbon particles. As carbon is very active for the two-electron pathway of the ORR forming hydroperoxide,[37,38] its presence in composite electrodes can greatly influence the measured number of electrons transferred and ORR activity of catalysts with low activities.[35,37,39−42] In addition, these thin-film oxide samples allow for the study of the role of surface termination on ORR kinetics.[34,43,44] Moreover, studying pure catalysts without the incorporation of conductive carbon enables the measure of charge transfer kinetics on the oxide surface using kinetically facile redox couples such as $[Fe(CN)_6]^{3-/4-}$ in solution,[45] independent from ORR kinetics measurements.[46] Having relatively thin oxide films on conductive substrates (Nb-doped $SrTiO_3$ or Pt) to facilitate charge transfer kinetics at the oxide surface is critical, as most manganese oxides are poor electronic conductors. For example, 200 nm of polycrystalline $LaMnO_3$ and $La_{0.8}Sr_{0.2}MnO_3$ films studied by Miyahara et al.[45] were found more resistive than a Pt surface, illustrated by the $[Fe(CN)_6]^{3-/4-}$ reaction. Some rotation dependence in current was still observed, considered by the authors to illustrate sufficient electronic conductivity.[45] However, we caution that hindered kinetics of $[Fe(CN)_6]^{3-/4-}$ suggests a comparable resistive component to the ORR.

3. KEY FACTORS INFLUENCING ORR KINETICS ON MANGANESE OXIDES

Although manganese oxides have been studied extensively, key factors that influence the specific ORR activity are not well-defined because it is not straightforward to compare across different studies where manganese oxides have been synthesized by a number of techniques such as electrochemical deposition,[47−51] hydrothermal methods,[21,52] soft chemical approaches,[41,42,53−55] annealing steps,[33,56] and electrochemical treatment.[52] Each technique results in considerably different crystal/particle size,[22] shape,[21] porosity,[57] and electronic conductivity.[58] Not only do these properties affect the mass activity of the oxides, but also they correlate with the electronic structure at the surface and thereby give rise to different specific activities.

Manganese in oxides adopt a variety of crystal structures and may exist in different valence states of 2+, 3+, and 4+, or mixtures thereof.[59] The crystal structures of manganese oxides most relevant to oxygen reduction are shown in Figure 3. Manganese dioxides can crystallize in different one-dimensional tunnel structures such as β-MnO_2 with 1 × 1 tunnels and space group $P42/mnm$ (ref 60; Figure 3A), Ramsdelite MnO_2 with 1 × 2 tunnels and space group $Pmna$ (Figure 3B), an intergrowth of these phases with both 1 × 1 and 1 × 2 tunnels referred to as electrolytic manganese dioxide (EMD),[61] and α-MnO_2 with 2 × 2 tunnels and space group $I4/mmm$ (Figure 3C).[62] β-MnO_2 is thermodynamically most stable at room temperature among all manganese oxides.[63,64] Another commonly studied manganese oxide is of the birnessite type (δ-MnO_2), which consists of layers of Mn octahedral in space group $C2/m$ (Figure 3D), containing some extent of group I cations between the layers and reducing some of the Mn to 3+. In reduced forms fully comprised of Mn^{3+}, γ-MnOOH has similar 1 × 1 tunnels[59] to β-MnO_2 with the space group $P2_1/C$ (ref 65; Figure 3E), where the Mn^{3+} is surrounded by edge-sharing octahedra of half O and half OH ligands, bixbyite α-Mn_2O_3 has corner-sharing octahedra, some of which are stretched with longer apical bonds due to Jahn−Teller distortion giving the orthorhombic space group $Pcab$ (ref 66; Figure 3F), and perovskites denoted $AMnO_3$ have corner-sharing octahedra and rare earth ions on the A site (Figure 3G). In further reduced forms, the spinel Mn_3O_4 forms a mixture of Mn^{2+} and Mn^{3+} found in tetrahedral and octahedral sites, respectively, with space group $Fd\bar{3}m$ (ref 67; Figure 3H).

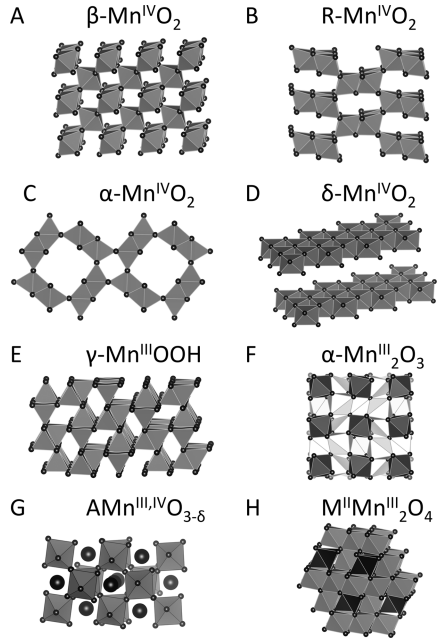

Figure 3. Illustration of the crystal structures of select common manganese oxides: (A) rutile β-$Mn^{IV}O_2$ (pyrolusite), (B) R-$Mn^{IV}O_2$ (ramsdelite), (C) α-$Mn^{IV}O_2$ (hollandite), (D) δ-$Mn^{IV}O_2$ (birnessite), (E) γ-$Mn^{III}OOH$ (manganite), (F) α-$Mn^{III}_2O_3$ (bixbyite), (G) $AMn^{III,IV}O_{3-\delta}$ (perovskite), and (H) $M^{II}Mn^{III}_2O_4$ (spinel, e.g Mn_3O_4 or $CoMn_2O_4$). Manganese is shown by gray octahedra, transition metals by black tetrahedra, oxygen by small black circles, and group II/lanthanide cations (denoted "A") as large black circles. For clarity, protons were omitted and the two crystallographic Mn sites of α-$Mn^{III}_2O_3$ are shown in different shades of gray.

3.1. Specific ORR Activity. Reports of specific activity are scarce in the literature. In this Review, we have calculated and compared specific activities for select manganese oxides based on reported currents at 0.8 or 0.7 V vs RHE and oxide surface areas (Table 1). Regardless of crystal structure, the manganese oxides surveyed in Table 1 containing Mn^{3+} appear to have higher specific activities than those containing exclusively Mn^{2+} or Mn^{4+}.

The presence of Mn^{3+} with some Mn^{4+} is a key to achieve high specific ORR activities in perovskites. Previous findings[11] have shown that having Mn valence slightly above 3+ can provide the highest specific ORR activities found for perovskite

DOI: 10.1021/acscatal.5b01444
ACS Catal. 2015, 5, 6021−6031

Table 1. Comparison of Mn-contained Oxides Catalysts at 0.8 V vs RHE from Previous Studies, Including Their Surface Area (SA), Specific ORR Activity (I_s), Mass ORR Activity (I_m), Number of Electron Transfer Indicated by Limiting Currents (n), and Their Crystal Structures[a]

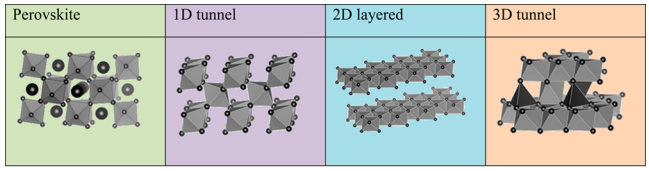

Material	SA (m^2/g)	I_s($\mu A/cm^2_{ox}$)	I_m(A/g_{ox})	n	Structure
$LaMnO_{3+d}$ [11]	0.5**	1300**	6.5	N/A	Perovskite
$La_{0.67}Sr_{0.33}MnO_3$ [36]	N/A	380	N/A	N/A	Perovskite
$La_{0.5}Ca_{0.5}MnO_3$ [11]	2.1**	330**	6.93	N/A	Perovskite
NP $CaMnO_{2.77}$ [19]	40	183.5	73.4	4.1	Perovskite
$La_{0.4}Sr_{0.6}MnO_3$* [22]	6.1	180	11	1.7	Perovskite
$La_{0.8}Sr_{0.2}MnO_3$ (820μg/cm^2 C)* [42]	16.7	150	25	1.6	Perovskite
MS $CaMnO_{2.76}$ [19]	36.4	126.8	46.2	4	Perovskite
NP $CaMnO_{2.90}$ [19]	38.5	115.3	44.4	4	Perovskite
MS $CaMnO_{2.50}$ [19]	37	98.0	36.3	3.9	Perovskite
$LaMnO_3$/NC [123]	11.6**	60	7	N/A	Perovskite
MS $CaMnO_{2.93}$ [19]	33.1	53.4	17.7	3.9	Perovskite
$LaMnO_3$/NSTO [34]	N/A	40	N/A	N/A	Perovskite
$La_{0.8}Sr_{0.2}MnO_{3-x}$/NSTO [43]	N/A	24	N/A	N/A	Perovskite
$La_{0.2}Sr_{0.8}MnO_3$* [22]	6	20	1.2	1.7	Perovskite
$La_{0.8}Sr_{0.2}MnO_{3-x}$/C [43]	4.4	14	0.62	N/A	Perovskite
$LaMn_{0.5}Ni_{0.5}O_3$ [11]	1.1**	13**	0.143	N/A	Perovskite
$LaMnO_3$ [11]	0.6**	13**	0.078	N/A	Perovskite
$LaMn_{0.5}Cu_{0.5}O_3$ [11]	1.1**	6.7**	0.0737	3.9	Perovskite
$La_{0.6}Ca_{0.4}Co_{0.5}Mn_{0.5}O_{3-x}$/C* [39]	10	6	0.6	2.3	Perovskite
$CaMnO_3$/C* [90]	67.5**	0.4**	0.27	3.27	Perovskite
$CaMnO_3$* [90]	67.5**	0.2**	0.135	3.18	Perovskite
$CaMnO_3$/NSTO [34]	N/A	0.1	N/A	N/A	Perovskite
Urchin $La_{0.8}Sr_{0.2}MnO_3$/C [20]	50	0.04	0.02	3.8-3.9	Perovskite
MnOOH/C (36 wt%) [124]	20.5**	3.6**	0.74	3.9	Corner-sharing
β-MnO_2 [15]	4.8	67	3.3	2.4	1D tunnel
α-MnO_2/C [21]	8	10	0.8	3.8	1D tunnel
α-MnO_2 [15]	112.5	6.4	7.2	3.7-4.2	1D tunnel
α-MnO_2 (nanorod_SF)* [99]	147	6	8.8	2.5	1D tunnel
α-MnO_2 (nanorod) [110]	19.5	2	0.39	3.89	1D tunnel
α-MnO_2 (nanotube) [110]	26	1	0.26	3.94	1D tunnel
α-Mn_2O_3* [41]	N/A	N/A	0.27	3.91	1D tunnel
γ-MnOOH* [41]	N/A	N/A	0.3	3.96	1D tunnel
MnO_2/C* [104]	N/A	N/A	100	2.3	1D tunnel
Mn_2O_3/C* [104]	N/A	N/A	10	1.5	1D tunnel
Mn_5O_8* [41]	N/A	N/A	0.25	3.75	1D tunnel
δ-MnO_2 [15]	25	6.7	1.7	1.7	2D layered
δ-MnO_2 [110]	62.5	0.4	0.25	3.03	2D layered
$H_{0.32}MnO_2$/GO [125]	N/A	N/A	0.22	~3.8	2D layered
Mn_3O_4/pGC [12]	N/A	700	N/A	~4	3D tunnel
Mn_2CoO_4 [78]	11	530	58	3.68	3D tunnel
$MnCo_2O_4$ [78]	36.7	30	11	3.51	3D tunnel
$Co_xMn_{3-x}O_4$-P/C (30 wt%) [80]	114	1.4	1.6	N/A	3D tunnel
$Co_xMn_{3-x}O_4$-B/C (30 wt%) [80]	108	1.2	1.3	N/A	3D tunnel
Mn_3O_4/C* [104]	N/A	N/A	30	1.5	3D tunnel
Mn_3O_4* [41]	N/A	N/A	0.26	3.8	3D tunnel

[a]The data were roughly estimated from CV curves or Tafel plots in 0.1 M KOH electrolyte, and the oxide surface areas were reported from BET measurements, unless specifically noted in the table. The materials were sorted by structures with different shadings (green, perovskites or other structures with corner-sharing octahedra; purple, 1D tunnel-structure oxides with edge-sharing octahedra; blue, 2D layered oxides with edge-sharing octahedra; orange, 3D tunnel structure with edge sharing octahedra). In the same structure group, the materials were sorted by specific ORR activity I_s. *Measurement was done in 1 M KOH electrolyte. **Surface area (SA) was reported from particle size estimation by SEM or TEM.

oxides (mixed with AB carbon) in basic solution (Figure 4A). The Mn valence state can be tuned in the perovskite structure by substitution of cations at the A-site, partial substitution of manganese for an aliovalent transition metal, and stoichiometry of oxygen ($3 \pm \delta$). Substituting divalent cations such as Sr^{2+} for La^{3+}, and thus oxidizing some Mn^{3+} to Mn^{4+}, increases the ORR activity.[11,36,68] For negligible oxygen nonstoichiometry in the $La_{1-x}Sr_xMnO_3$ (LSMO) perovskite crystal structure at room temperature, the nominal average valence of octahedrally coordinated Mn can be estimated by charge conservation. In a study of LSMO powders with six Sr substitutions (on glassy carbon),[22] $La_{0.4}Sr_{0.6}MnO_3$ (nominal valence $Mn^{3.6+}$) has the highest ORR activity in 1 M KOH (180 $\mu A/cm^2_{ox}$ at 0.8 V vs RHE), over an order of magnitude improvement compared to other LSMO.[22] This finding is supported by a recent study of epitaxial thin films of the pseudocubic $(001)_{pc}$ orientation,[36] where $La_{0.77}Sr_{0.33}MnO_3$ (no exposed substrate) has the highest ORR activity in 0.1 M KOH (380 $\mu A/cm^2_{ox}$ at 0.8 V vs RHE) among seven Sr substitutions. It is proposed that mixed Mn valence results in favorable charge transfer to adsorbed oxygen and renders high ORR activity as probed by a fast redox couple at 1.2 V vs RHE.[36] On the other hand, having largely Mn^{4+} results in low ORR activities as shown by the poor activity of $LaNi_{0.5}Mn_{0.5}O_3$ (mixed with AB carbon in 0.1 M KOH), where Mn ions are 4+ accompanied by Ni^{2+} ions (Figure 4A),[11] as well as the low activity of $CaMnO_3$ thin films with Mn^{4+} compared to $LaMnO_3$ (Figure 4B).[34] Moreover, tuning Mn valence via oxygen nonstoichiometry has shown that having some Mn^{4+}, but no more than Mn^{3+}, is essential for high ORR activities. For example, $LaMnO_{3+\delta}$ (mixed with AB carbon in 0.1 M KOH),[69] with ~20% of the Mn in the 4+ oxidation state, has high specific ORR activity (1.3 mA/cm^2_{ox} at 0.8 V vs RHE), greater than that of stoichiometric $LaMnO_3$.[11] A secondary example is that of $CaMnO_{2.77}$ (mixed with Vulcan carbon in 0.1 M KOH) with $Mn^{3.5+}$, which has specific ORR activity ~2× improved (184 $\mu A/cm^2_{ox}$ at 0.8 V vs RHE) compared to $CaMnO_{2.90}$ with an average valence of $Mn^{3.9+}$,[19] where the oxygen nonstoichiometry was tuned by thermal reduction.

The critical role of Mn^{3+} in achieving high ORR activity can be rationalized by considering how the electronic structure

DOI: 10.1021/acscatal.5b01444
ACS Catal. 2015, 5, 6021−6031

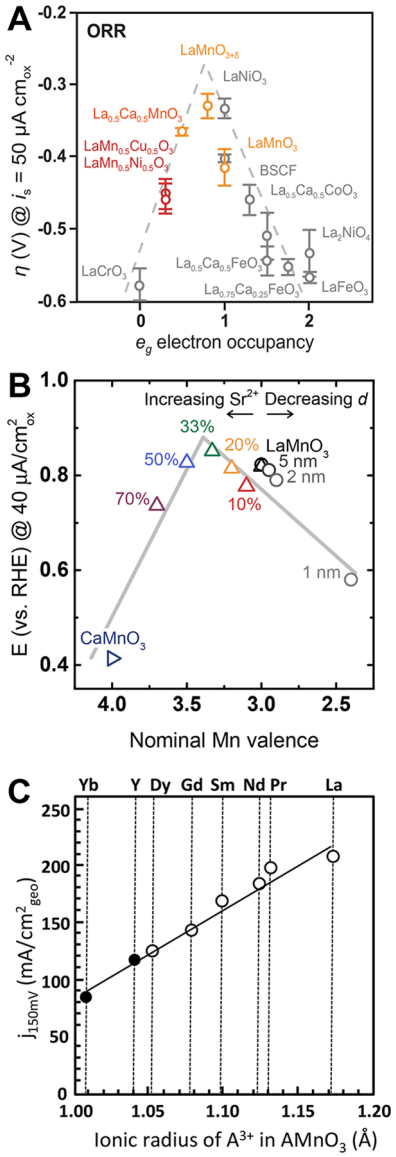

Figure 4. (A) Volcano trend of ORR activity of powder perovskites (surface area from scanning electron micrograph, SEM) with estimated e_g occupancy of the transition metal ions as reported previously.[11,24] (B) Oxygen reduction activity at 40 μA/cm^2 current of Mn-containing perovskite films grown epitaxially on a Nb:SrTiO$_3$ substrate.[34,36] The nominal valence is estimated by the % Sr^{2+} substitution for La^{3+} in $La_{(1-x)}Sr_xMnO_3$ (colored triangles)[36] and a trend in reduced valence by X-ray absorption spectroscopy (XAS) with reduced film thickness (gray circles).[34] (C) ORR activity as a function of the ionic radius of lanthanide (A^{3+}) in $AMnO_{3\pm\delta}$ measured in GDE.[70] All oxides had a comparable surface area of 13 ± 1 m^2/g. Solid symbols required an additional annealing step for comparable surface area. The panels of this figure were reproduced from (A) ref 11 with permission from Nature Publishing Group, copyright 2011, and (C) ref 70 with permission from the Electrochemical Society, copyright 1996.

interacts with adsorbed oxygen, assuming the valence of Mn at the surface reflects that in bulk for well-crystallized materials. In a truncated octahedral environment (such as the (001) surface of a perovskite), the e_g antibonding orbitals of Mn^{3+} directly overlap with apically adsorbed oxygen, through which the e_g filling can influence the binding strength of O_2 on the Mn^{3+} ions. Following the well-known four-step proton−electron-coupled reaction mechanism for the ORR (Figure 5A):[11,24,71]

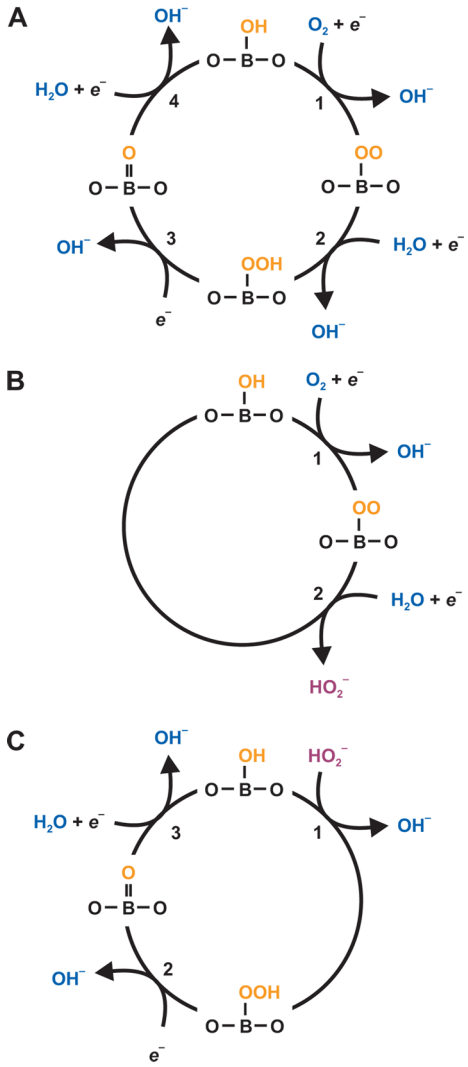

Figure 5. Possible pathways of electrolytic oxygen and peroxide reduction. Orange denotes species on the catalyst surface, and blue/purple denotes species in solution. (A) Four-electron pathway reducing O_2 to hydroxide;[11,24,71] (B) two-electron pathway reducing O_2 to peroxide;[87] (C) two-electron reduction of peroxide.[88]

(1) O_2 adsorbs as OO^{2-} onto a Mn site, displacing an OH^- group from the surface, (2) the peroxo group is protonated to form OOH^-, (3) an OH^- group is removed from the surface, leaving a superoxo O^{2-} group, which (4) is protonated to reform the hydroxyl-covered starting surface. The rate of oxygen adsorption to replace OH^- adsorbed on the Mn ion site (step 1) is considered to limit ORR kinetics on metal oxides, where the oxygen adsorption strength on the Mn ion site can be dictated by the electron filling of the e_g orbitals of metal ions.[11,72] Thus, going from zero e_g electrons in Mn^{4+} to one e_g electron in Mn^{3+} decreases the strength of oxygen adsorption[73] and facilitates the exchange kinetics of OH^- by O_2 on the Mn site, leading to an optimum ORR activity at an e_g filling slightly less than one and corresponding to mixed $Mn^{3+/4+}$ in $LaMnO_{3+\delta}$.[11]

Several publications[34,36,43,74] have shown that ORR activities of epitaxial oxide thin films can be comparable to those of ink-casted oxide powders. However, in contrast to 15 nm epitaxial films on a conductive substrate discussed above,[36] catalyst−support interactions have been found to play a notable role in

DOI: 10.1021/acscatal.5b01444
ACS Catal. 2015, 5, 6021−6031

the study of thinner $(001)_{pc}$-oriented $LaMnO_{3\pm\delta}$. Decreasing the film thickness from 10 to 1 nm led to a dramatic reduction in activity, attributed in part to charge-transfer from the Nb:$SrTiO_3$ substrate, reducing some of the Mn to a less active 2+ valence state.[34] Thus, an activity volcano for solely Mn perovskites can be generated in which the activity is tuned by orders of magnitude with the valence state via A-site substitution and substrate effects, where a mix of $Mn^{3+/4+}$ valence is most active (Figure 4B).

In addition to e_g filling as a primary factor governing ORR activity, the covalency of the Mn−O bond can influence specific ORR activity but to a lesser extent,[11] as Mn−O hybridization can mediate electron transfer[46] to oxygen.[11,75] This concept is supported by the fact that ORR activity of $AMnO_{3\pm\delta}$ increases with increasing the A-site cation radius, which is accompanied by increasing basicity of the A-site[76,77] and covalency of Mn−O bonds (Figure 4C),[70] provided that the oxygen nonstoichiometry of these $AMnO_{3\pm\delta}$ oxides does not change significantly. Such an effect has also been observed in comparing ABO_3 perovskites at fixed e_g occupancy,[11] where increasing the B−O covalency (B = Mn, Co, and Ni) increased ORR activity.

The critical role of Mn^{3+} in octahedral sites to provide high specific ORR activity is further supported by studies of the spinel structure, $M^{II}M^{III}{}_2O_4$, which incorporates Mn^{2+} at tetrahedral sites and Mn^{3+} at octahedral sites (Figure 3H). Tetragonal $CoMn_2O_4$ with octahedral Mn^{3+} (mixed with Vulcan carbon in 0.1 M KOH, ref 78) has shown to be over an order of magnitude more active than cubic $MnCo_2O_4$,[79,80] with tetrahedral Mn^{2+} (activities in Table 1), further supporting that octahedrally coordinated Mn^{3+} is needed to catalyze ORR kinetics. Unifying both motifs, the spinel Mn_3O_4 (refs 12 and 47) can exhibit specific activities of up to 700 $\mu A/cm^2{}_{ox}$ at 0.8 V vs RHE.

Considering other binary oxides, the β-phase (β-MnO_2) is an order of magnitude more active (67 $\mu A/cm^2{}_{ox}$ at 0.8 V vs RHE) than α-MnO_2 or δ-MnO_2 (6−7 $\mu A/cm^2{}_{ox}$ at 0.8 V vs RHE; Table 1).[15] However, we caution that other activity-determining parameters, such as oxygen defects[81] and the corresponding Mn valence,[82,83] in addition to the reaction product (OH^- or HO_2^-) might also differ for these phases. This is emphasized by the contrasting report of activity decreasing in the order of $\alpha > \beta > \gamma$-MnO_2 reported in a comparison of nanowires with more comparable morphology and size, but lacking a report of specific surface areas.[21]

3.2. The Number of Electrons Transferred in ORR. The ORR can proceed to form hydroxide or hydroperoxide in alkaline media. In the direct pathway, four electron transfers occur on the same catalytic site to form hydroxide (Figure 5A). In the series pathway, there is an initial two-electron reduction of oxygen to peroxide (Figure 5B), proceeding by the same pathway as steps 1 and 2 in the four-electron reduction in Figure 5A; however difficulty in cleaving the O−O bond results in desorption of the protonated group as hydroperoxide (HO_2^-). This can be followed by either a two-electron reduction of readsorbed hydroperoxide to hydroxide (Figure 5C) via a superoxo O^{2-} intermediate or by the peroxide disproportionation reaction that produces O_2 in half the original amount via a chemical step, which can be subsequently reduced to peroxide in an "apparent" four-electron process (reinitiating the process of Figure 5B). The four-electron ORR is desirable for energy conversion applications, and the generation of peroxide during the ORR needs to be minimized as it can chemically attack catalysts,[25,84] catalyst support,[38] and ion-conducting membranes in fuel cells.[85,86]

The presence of Mn^{3+} with some Mn^{4+} is key not only to facile ORR kinetics but also to increasing the number of electrons transferred and the fraction of hydroxide (four electron) relative to peroxide.[22] Koutecky−Levich analysis illustrates that the perovskite $LaCu_{0.5}Mn_{0.5}O_3$ (Mn^{3+}) supported on high surface area carbon exhibits a direct or apparent four-electron process for the ORR,[14] and RRDE measurements show the percent of hydrogen peroxide production on carbon-supported $La_{0.8}Sr_{0.2}MnO_3$,[87] $LaMnO_3$,[89] and $LaNi_{0.5}Mn_{0.5}O_3$[89] is <10%. A-site substitution in perovskites can also increase the number of electrons transferred associated with ORR and the fraction of hydroxide (four electron) relative to peroxide, with maximum n observed intermediate $Mn^{3+/4+}$ mixtures.[22] This is in contrast to perovskites of primarily Mn^{4+}, such as $CaMnO_3$ and $CaMn_{0.85}Ru_{0.15}O_3$, which produce around 30% peroxide,[90] suggesting the presence of Mn^{3+} (with a small amount of Mn^{4+}) maximizes the four-electron process for the ORR.

The stoichiometry of different binary manganese oxides (dictating manganese valence state) has also been shown to influence the number of electrons transferred by Koutecky−Levich analysis and HO_2^- detected via RRDE measurements. The limiting currents in Figure 2B suggest that α-MnO_2 catalyzes the ORR by close to a four-electron pathway (oxygen to hydroxide) while the number of electrons transferred in the ORR on δ-MnO_2 and β-MnO_2 is less than 4.[15] Mn^{3+}-based oxides (supported on gold in 0.1 M KOH) such as Mn_2O_3 and γ-MnOOH yielded <5% peroxide while more reduced forms such as Mn_5O_8 and Mn_3O_4 with Mn^{2+} and Mn^{3+} have peroxide yields closer to 15%.[41] Doping MnO_x with metal cations Ni^{2+} and Mg^{2+} (mixed with carbon black in 0.1 M KOH) has also demonstrated improved selectivity toward the four-electron pathway,[84] which was attributed to stabilizing intermediate Mn^{3+}/Mn^{4+} species.[53] Tetragonal $CoMn_2O_4$ with octahedral Mn^{3+} (ref 78) has been shown by Koutecky−Levich analysis to exhibit an electron transfer number close to 4, higher than that of the cubic $MnCo_2O_4$,[79,80] with tetrahedral Mn^{2+}. Thus, studies of both binary and ternary manganese oxides point to Mn^{3+}, possibly including some Mn^{4+} (but not Mn^{2+}) as key to catalyzing the four-electron process. We caution, however, that common support materials such as carbon[37,38] and gold[91] are active for oxygen reduction to hydroperoxide ($2e^-$) at large overpotentials and may influence the observed number of electrons transferred.

3.3. The Activity for Peroxide Disproportionation. Manganese oxides can disproportionate peroxide chemically to generate molecular oxygen and water or hydroxyl species, where oxygen can be further reduced. Therefore, peroxide disproportionation kinetics on oxides can play an important role in ORR kinetics. MnO_2,[92,93] MnOOH,[41] and mixed oxides such as spinels and perovskites[94,95] are active toward hydrogen peroxide decomposition, which can influence the number of apparent electrons transferred during ORR.

The activity toward hydrogen peroxide decomposition can be influenced by Mn valence in oxides. Partial substitution of La^{3+} by Sr^{2+} or Ca^{2+} in $La_{(1-x)}A_xMnO_3$ (A = Sr, Ca) has been shown to increase the activity toward peroxide decomposition.[96,97] In $La_{(1-x)}Sr_xMnO_3$, the activity for the HO_2^- decomposition was a maximum at x = 0.8, the highest Sr (and Mn^{4+}) content tested.[96] The corresponding increase in activation energy with activity suggested the compensation effect,[98] thus Mn^{4+} sites are considered active for peroxide decomposition.[96,97] We note,

DOI: 10.1021/acscatal.5b01444
ACS Catal. 2015, 5, 6021−6031

however, that such studies did not consider chemistries with fully Mn^{4+} character.

Comparison of α-MnO_2 nanorods[99] prepared to yield a range of average Mn oxidation states (3.91, 3.85, and 3.73+) found a successive increase in the rate of hydrogen peroxide decomposition (0.14 to 0.53 $s^{-1}g^{-1}$), which exceeded the difference in surface areas (90−140 m^2/g). This paralleled the increase in the limiting current and therefore the number of electrons transferred as measured by RDE, as well as the exchange current density (8.1 to 10 $\mu A/cm^2_{disk}$ at constant loading).[99] Therefore, having a considerable amount of Mn^{3+} in addition to Mn^{4+} is necessary to promote peroxide disproportionation kinetics and thus ORR kinetics. This hypothesis is supported by the observation that Ni-substituted α-MnO_2 with comparable surface area to Ni-free α-MnO_2 exhibited a 4-fold increase in the rate of hydrogen peroxide decomposition, a slight increase in limiting current, and a 2-fold increase in exchange current density.[99]

It is interesting to contrast peroxide decomposition activity with ORR kinetics, where a large number of Mn^{3+} sites (ideally mixed with a smaller amount of Mn^{4+} sites) are needed to give high ORR activity. Having Mn^{3+} catalyzing ORR and Mn^{4+} catalyzing peroxide decomposition, which facilitates the apparent four-electron process, is in agreement with the following observations: First, the HO_2^- production from $La_{(1-x)}Sr_xMnO_3$ during the ORR is minimized with moderate incorporation of Sr (closest to four-electron process for x = 0.6).[22] Second, $La_xCa_{0.4}MnO_3$ has shown largely four-electron transfer for ORR, with decreased peroxide production as x decreases from 0.6 to a nonstoichiometric, cation deficient composition.[100] Third, $CaMnO_x$ with intermediate $Mn^{3+/4+}$ composition has shown an increased number of electrons transferred in comparison to Mn^{3+} or Mn^{4+} end members.[101]

While the two-electron reduction of oxygen to peroxide can occur on carbon[102,103] or manganese oxides,[103,104] the catalytic activity for peroxide disproportionation has been attributed solely to manganese oxides to give rise to apparent four-electron reduction of oxygen.[41,104] This hypothesis is supported by a study from Calegaro et al.[105] where increasing the manganese oxide load (mixture of β-MnO_2 and Mn_2O_3) relative to carbon was shown by Koutecky−Levich analysis to increase the number of electrons transferred from 2.1 to 2.8.[105] Further support comes from the fact that the efficacy of this process increases with decreasing scan rate in cyclic voltammetry, attributed to increased residence time for the manganese oxides to regenerate sufficient O_2 from disproportionation.[41]

Besides chemical disproportionation, there is a second route to increase the number of electrons transferred while involving peroxide intermediates: the electrochemical reduction of peroxide. Various types of high-surface area carbon have been added to enhance the conductivity of composite electrodes in previous studies.[39,40,42] Due to the two-electron reduction of oxygen to peroxide on carbon, one would expect an increase of the peroxide yield when carbon is added. However, $La_{0.8}Sr_{0.2}MnO_3$ alone (supported on glassy carbon) produced around 40% peroxide,[22,87] while incorporation of carbon black reduced the production to <10%; increased loading of both catalyst and support further reduced HO_2^- production.[87] This suggests the oxide catalyst alone may not have sufficient conductivity to reduce peroxide produced on the glassy carbon substrate, which can be overcome by mixing with high surface area carbon for conductivity.

3.4. ORR Mass Activity. While specific activity of the ORR on manganese oxides can be influenced greatly by oxidation state, e_g occupancy and covalency, ORR mass activity is also affected by specific oxide surface area (m^2/g_{oxide}). A survey of mass activities from different manganese oxides can be found in Table 1, where mass activity trends among these oxides are discussed below. Most perovskites need to be crystallized with high annealing temperatures,[106] resulting in micron-sized particles with low specific surface areas (<10 m^2/g). While there have been some efforts to make perovskite nanoparticles,[19,20,101,106] the majority of reported perovskite catalysts have comparably large particle sizes and low to moderate mass activities (Table 1). On the other hand, binary Mn-based oxides can be formed at lower temperatures,[80] thus aiding in the production of nanostructured particles with high surface areas exceeding 30 m^2/g (ref 11). Among materials supporting four-electron reduction, perovskite $CaMnO_{3-\delta}$ nanoparticles remarkably exhibit the highest mass activity (~70 A/g_{oxide}),[19] and spinel $CoMn_2O_4$ has the second highest mass activity (60 A/g_{oxide}).[78] Nanostructured 1D-tunnel-structure manganese dioxides have considerably lower mass activity, among which α-MnO_2 is the most active (7 A/g_{oxide}).[15] Although MnO_2/C (predominantly β phase with some Mn_2O_3) has been shown to have a mass activity of 100 A/g_{oxide},[104] the number of electrons transferred is close to two, yielding largely peroxide, which is highly undesirable for energy conversion applications.

Generally speaking, surveying average Mn valences ranging from 2.6 to 4 in both powders,[41,107,108] and nanorods,[52,109] Mn in the higher oxidation state of $Mn^{3+/4+}$ has been found most active by mass, similar to findings from the specific activity discussed above. The ORR mass activities of manganese oxides[41,107] increased with Mn oxidation state from 1.2 to 1.4 A/g_{oxide} at 0.7 V vs RHE in the sequence of Mn_5O_8 < Mn_3O_4 < Mn_2O_3 < γ-MnOOH.[41] Comparison with other studies suggest a mass activity of MnO_2 allotropes 2−100 times greater[15,21,110,111] than more reduced oxides.

4. TOWARD UNDERSTANDING OF MANGANESE OXIDE SURFACES DURING THE ORR

With the above discussion concerning the role of Mn valence in ORR activity from the perspective of characterization preceding catalysis, we turn next to review the surface of manganese oxides during ORR conditions. A computed E-pH (Pourbaix)[112] diagram of MnO_x from density functional theory (DFT) calculations shows that the β-MnO_2 phase with low-index (110) facet and partial coverage by adsorbed O is stable at the equilibrium potential of the ORR at 1.23 V vs RHE (Figure 6A).[113] Polarizing to the onset of the ORR (0.83 V vs RHE) leads to the Mn_2O_3 (110) surface covered with a half monolayer of adsorbed OH as the most stable, which can be further reduced to a clean Mn_3O_4 (001) surface at lower potentials of 0.69 V vs RHE.[113] DFT calculations suggest that the ORR may occur through an associative mechanism, where O_2 adsorbs intact with intermediates as in Figure 5a (in contrast to a direct dissociative/recombination mechanism), on surfaces of Mn_2O_3 (110) and Mn_3O_4 (001) stable under ORR-relevant conditions (termed "self-consistent"). The computed overpotential was highly dependent on the stabilization of intermediates through hydrogen bonds with water molecules.[113] Such calculations have found a theoretical onset potential of 0.4 V comparable to that measured experimentally for α-Mn_2O_3.[113]

DOI: 10.1021/acscatal.5b01444
ACS Catal. 2015, 5, 6021−6031

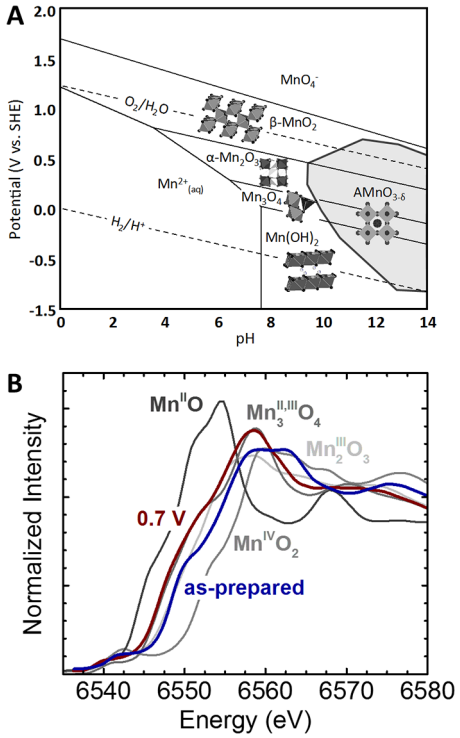

Figure 6. (A) Simplified Pourbaix diagram of phases predicted for ORR conditions by DFT for binary manganese oxide,[113] including the stable region for the perovskite $LaMnO_3$ (shaded area).[114] Within the stable regions, surfaces at lower potentials are clean or covered with *OH, and those at higher potentials covered in *O. (B) In situ X-ray absorption[115] at the Mn K-edge (fluorescence yield mode) of electrodeposited MnO_x at 0.7 V vs RHE, as-deposited and relevant references. Adapted from ref 113 with permission from the PCCP Owner Societies, copyright 2012, and from ref 115 with permission from the American Chemical Society, copyright 2013.

For ternary oxides such as the perovskite $LaMnO_3$, DFT has assessed the relative stability of different terminations of the (001) facet as a function of pH and potential.[114] Near the equilibrium potential of the ORR at 1.23 V vs RHE, an oxidized Mn surface is most stable with some Mn vacancies, where all Mn atoms are fully coordinated to O. Under ORR conditions, the surface becomes protonated, being fully saturated with OH groups for potentials of <0.76 V vs RHE. At even lower potentials of <0.58 V vs RHE, the surface groups are reduced, leaving a bare MnO_2 (001) facet. These changes in character of the surface adsorbates are linked to subsequent reduction of the Mn valence state. The energetics of ORR intermediates computed on this surface are in agreement with the ORR proceeding under such applied potentials.

The valence state of Mn has been shown experimentally to change as a function of ORR potential.[115−117] In situ evaluation of catalysts with hard X-ray absorption spectroscopy at the Mn K-edge highlights the reduction of Mn under ORR conditions, as predicted by DFT, with highly active materials having $Mn^{3+/4+}$ redox near the ORR onset.[117] Annealing β-MnO_2 particles on Vulcan carbon (X-72) to an ex situ stoichiometry of Mn_2O_3/C and Mn_3O_4/C eliminated a redox feature coincident with the ORR half-wave potential (0.75 V vs RHE), leading to reduced ORR activity, which can be attributed to thermal reducing Mn to a 3+ valence, prohibiting $Mn^{3+/4+}$ redox during the ORR.[117]

More recent in situ XAS studies at the Mn K-edge of $Mn^{III}O_x$ films electrodeposited on an Au/Si_3N_4 window demonstrate a lack of $Mn^{3+/4+}$ redox at the ORR onset,[115] in agreement with ex situ L-edge studies which show thermal Mn^{3+} oxides cannot be reoxidized in solution.[33] Partial reduction of Mn^{3+} was observed for an ORR-relevant potential of 0.7 V vs RHE in 0.1 M KOH (Figure 6B),[115] where disordered Mn_3O_4 was detected in operando by the XAS fine structure, displaying reduced peak intensity compared to the crystalline reference.[115] The facile reduction of these $Mn^{III}O_x$ films to Mn_3O_4 throughout the film and their high specific activity of 700 $\mu A/cm^2$ at 0.8 V vs RHE, quantified in a parallel study on glassy carbon substrates,[12] contrasts limited reduction to Mn_3O_4 during the ORR reported by others.[118,119] The detection of Mn_3O_4 might be explained by the findings of DFT studies,[113] where small crystals favor the formation of the low surface energy phase Mn_3O_4, compared to Mn_2O_3.[120] Therefore, further in situ characterization of different manganese oxides prepared by different synthesis routes is needed to provide insights into the physical origin of the differences in observed activities.

5. CONCLUSIONS AND OUTLOOK

Through studies of crystal structures like perovskites ($AMn^{III,IV}O_{3\pm\delta}$) and spinels ($M^{II}M^{III}{}_2O_4$), where the crystal structure can be maintained through inclusion of a wide range of chemistries, the specific ORR activities of catalysts with a range of Mn valence state can be compared. Mn^{3+} in octahedral coordination is a critical player in the ORR, where incorporation of some Mn^{4+} can improve charge transfer to adsorbed oxygen and promote catalysis. It is desirable to proceed via the four-electron process to form hydroxide and avoid the less efficient two-electron path to hydroperoxide. The more reducible α-MnO_2 with open structure proceeds via an apparent four-electron process, in contrast to other polymorphs (and the carbon support), which primarily reduce O_2 to the hydroperoxide ion. For perovskites, a primarily four-electron process is observed. By comparing materials which operate by the two- and four-electron process, it is shown that the presence of $Mn^{3+/4+}$ mixed valence promotes cleavage of the O_2 bond and complete reduction to OH^-. One factor may be increased peroxide decomposition by Mn^{4+}; however further studies are needed to distinguish between the apparent and direct four-electron process.

The active valence state during and resulting from the ORR has been further probed by spectroscopic and computational methods. Computations of simple manganese oxides have shown the Mn^{3+} valence state is stable under ORR conditions. In situ evaluation of catalysts with hard X-ray absorption spectroscopy highlights the reduction of Mn under ORR conditions, with highly active materials having $Mn^{3+/4+}$ redox near the ORR onset. Future in situ measurements utilizing soft X-rays could provide increased chemical sensitivity, evaluating the Mn valence by X-ray absorption[121] or probing oxygen speciation with techniques like ambient pressure X-ray photoelectron spectroscopy.[122] A promising route to elucidate the details of the ORR mechanism entails eliminating support surfaces exposed to the electrolyte through the study of epitaxial thin film electrodes, which can serve as well-defined model surfaces.[36] This recent trend in electrode geometry offers great promise in separating the effect of the substrate and the manganese oxide surface in ORR electrocatalysis,[34,45] establishing the role of oxide conductivity and distinguishing between direct and apparent four-electron processes. In combination

DOI: 10.1021/acscatal.5b01444
ACS Catal. 2015, 5, 6021−6031

with electroanalytical measurements and in situ spectroscopy, this could yield insight into the ORR mechanism with unprecedented clarity.

AUTHOR INFORMATION

Corresponding Authors

*E-mail: kastoerz@mit.edu.
*E-mail: shaohorn@mit.edu.

Notes

The authors declare no competing financial interest.

ACKNOWLEDGMENTS

This work was supported in part by the MRSEC Program of the National Science Foundation under award number DMR-0819762 and the Skoltech-MIT Center for Electrochemical Energy Storage. K.A.S. was supported in part by the National Science Foundation Graduate Research Fellowship under Grant no. DGE-1122374. Use of the National Synchrotron Light Source, Brookhaven National Laboratory, was supported by the U.S. Department of Energy, Office of Science, Office of Basic Energy Sciences, under contract no. DE-AC02-98CH10886. We thank Dr. Azzam N. Mansour for providing Mn K-edge reference spectra and Julius Scholz for measuring glassy carbon.

REFERENCES

(1) Gasteiger, H. A.; Kocha, S. S.; Sompalli, B.; Wagner, F. T. *Appl. Catal., B* **2005**, *56*, 9−35.
(2) Armand, M.; Tarascon, J. M. *Nature* **2008**, *451*, 652−657.
(3) Chen, J.; Cheng, F. *Acc. Chem. Res.* **2009**, *42*, 713−723.
(4) Cao, R.; Lee, J.-S.; Liu, M.; Cho, J. *Adv. Energy Mater.* **2012**, *2*, 816−829.
(5) Park, M.; Sun, H.; Lee, H.; Lee, J.; Cho, J. *Adv. Energy Mater.* **2012**, *2*, 780−800.
(6) Stephens, I. E. L.; Bondarenko, A. S.; Gronbjerg, U.; Rossmeisl, J.; Chorkendorff, I. *Energy Environ. Sci.* **2012**, *5*, 6744−6762.
(7) Cheng, F.; Chen, J. *Chem. Soc. Rev.* **2012**, *41*, 2172−2192.
(8) Morozan, A.; Jousselme, B.; Palacin, S. *Energy Environ. Sci.* **2011**, *4*, 1238−1254.
(9) Wang, B. *J. Power Sources* **2005**, *152*, 1−15.
(10) Jaouen, F.; Proietti, E.; Lefevre, M.; Chenitz, R.; Dodelet, J.-P.; Wu, G.; Chung, H. T.; Johnston, C. M.; Zelenay, P. *Energy Environ. Sci.* **2011**, *4*, 114−130.
(11) Suntivich, J.; Gasteiger, H. A.; Yabuuchi, N.; Nakanishi, H.; Goodenough, J. B.; Shao-Horn, Y. *Nat. Chem.* **2011**, *3*, 546−550.
(12) Gorlin, Y.; Chung, C.-J.; Nordlund, D.; Clemens, B. M.; Jaramillo, T. F. *ACS Catal.* **2012**, *2*, 2687−2694.
(13) Vesborg, P. C. K.; Jaramillo, T. F. *RSC Adv.* **2012**, *2*, 7933−7947.
(14) Suntivich, J.; Gasteiger, H. A.; Yabuuchi, N.; Shao-Horn, Y. *J. Electrochem. Soc.* **2010**, *157*, B1263−B1268.
(15) Meng, Y.; Song, W.; Huang, H.; Ren, Z.; Chen, S.-Y.; Suib, S. L. *J. Am. Chem. Soc.* **2014**, *136*, 11452−11464.
(16) Yeager, E. *J. Mol. Catal.* **1986**, *38*, 5−25.
(17) Siahrostami, S.; Verdaguer-Casadevall, A.; Karamad, M.; Deiana, D.; Malacrida, P.; Wickman, B.; Escudero-Escribano, M.; Paoli, E. A.; Frydendal, R.; Hansen, T. W.; Chorkendorff, I.; Stephens, I. E. L.; Rossmeisl, J. *Nat. Mater.* **2013**, *12*, 1137−1143.
(18) Rankin, R. B.; Greeley, J. *ACS Catal.* **2012**, *2*, 2664−2672.
(19) Du, J.; Zhang, T.; Cheng, F.; Chu, W.; Wu, Z.; Chen, J. *Inorg. Chem.* **2014**, *53*, 9106−9114.
(20) Jin, C.; Cao, X.; Zhang, L.; Zhang, C.; Yang, R. *J. Power Sources* **2013**, *241*, 225−230.
(21) Cheng, F.; Su, Y.; Liang, J.; Tao, Z.; Chen, J. *Chem. Mater.* **2010**, *22*, 898−905.
(22) Tulloch, J.; Donne, S. W. *J. Power Sources* **2009**, *188*, 359−366.
(23) Trasatti, S.; Petrii, O. A. *Pure Appl. Chem.* **1991**, *63*, 711.
(24) Hong, W. T.; Risch, M.; Stoerzinger, K. A.; Grimaud, A.; Suntivich, J.; Shao-Horn, Y. *Energy Environ. Sci.* **2015**, *8*, 1404−1427.
(25) Bidault, F.; Brett, D. J. L.; Middleton, P. H.; Brandon, N. P. *J. Power Sources* **2009**, *187*, 39−48.
(26) Ng, J. W. D.; Gorlin, Y.; Nordlund, D.; Jaramillo, T. F. *J. Electrochem. Soc.* **2014**, *161*, D3105−D3112.
(27) Gloaguen, F.; Andolfatto, F.; Durand, R.; Ozil, P. *J. Appl. Electrochem.* **1994**, *24*, 863−869.
(28) Mayrhofer, K. J. J.; Strmcnik, D.; Blizanac, B. B.; Stamenkovic, V.; Arenz, M.; Markovic, N. M. *Electrochim. Acta* **2008**, *53*, 3181−3188.
(29) Treimer, S.; Tang, A.; Johnson, D. C. *Electroanalysis* **2002**, *14*, 165−171.
(30) Sipos, P. M.; Hefter, G.; May, P. M. *J. Chem. Eng. Data* **2000**, *45*, 613−617.
(31) Davis, R. E.; Horvath, G. L.; Tobias, C. W. *Electrochim. Acta* **1967**, *12*, 287−297.
(32) Paulus, U. A.; Schmidt, T. J.; Gasteiger, H. A.; Behm, R. J. *J. Electroanal. Chem.* **2001**, *495*, 134−145.
(33) Gorlin, Y.; Nordlund, D.; Jaramillo, T. F. *ECS Trans.* **2013**, *58*, 735−750.
(34) Stoerzinger, K. A.; Risch, M.; Suntivich, J.; Lü, W. M.; Zhou, J.; Biegalski, M. D.; Christen, H. M.; Ariando; Venkatesan, T.; Shao-Horn, Y. *Energy Environ. Sci.* **2013**, *6*, 1582−1588.
(35) Arul Raj, I.; Vasu, K. I. *Int. J. Hydrogen Energy* **1990**, *15*, 751−756.
(36) Stoerzinger, K. A.; Lü, W.; Li, C.; Ariando; Venkatesan, T.; Shao-Horn, Y. *J. Phys. Chem. Lett.* **2015**, *6*, 1435−1440.
(37) Tatapudi, P.; Fenton, J. M. *J. Electrochem. Soc.* **1993**, *140*, L55−L57.
(38) Trogadas, P.; Fuller, T. F.; Strasser, P. *Carbon* **2014**, *75*, 5−42.
(39) Malkhandi, S.; Trinh, P.; Manohar, A. K.; Jayachandrababu, K. C.; Kindler, A.; Surya Prakash, G. K.; Narayanan, S. R. *J. Electrochem. Soc.* **2013**, *160*, F943−F952.
(40) Liang, Y.; Wang, H.; Diao, P.; Chang, W.; Hong, G.; Li, Y.; Gong, M.; Xie, L.; Zhou, J.; Wang, J.; Regier, T. Z.; Wei, F.; Dai, H. *J. Am. Chem. Soc.* **2012**, *134*, 15849−15857.
(41) Mao, L.; Zhang, D.; Sotomura, T.; Nakatsu, K.; Koshiba, N.; Ohsaka, T. *Electrochim. Acta* **2003**, *48*, 1015−1021.
(42) Poux, T.; Napolskiy, F. S.; Dintzer, T.; Kéranguéven, G.; Istomin, S. Y.; Tsirlina, G. A.; Antipov, E. V.; Savinova, E. R. *Catal. Today* **2012**, *189*, 83−92.
(43) Risch, M.; Stoerzinger, K. A.; Maruyama, S.; Hong, W. T.; Takeuchi, I.; Shao-Horn, Y. *J. Am. Chem. Soc.* **2014**, *136*, 5229−5232.
(44) Komo, M.; Hagiwara, A.; Taminato, S.; Hirayama, M.; Kanno, R. *Electrochemistry* **2012**, *80*, 834−838.
(45) Miyahara, Y.; Miyazaki, K.; Fukutsuka, T.; Abe, T. *J. Electrochem. Soc.* **2014**, *161*, F694−F697.
(46) Matsumoto, Y.; Yoneyama, H.; Tamura, H. *J. Electroanal. Chem. Interfacial Electrochem.* **1977**, *83*, 245−249.
(47) Gorlin, Y.; Jaramillo, T. F. *J. Am. Chem. Soc.* **2010**, *132*, 13612−13614.
(48) Lin, H. Y.; Sun, Y. P.; Weng, B. J.; Yang, C. T.; Suen, N. T.; Liao, K. H.; Huang, Y. C.; Ho, J. Y.; Chong, N. S.; Tang, H. Y. *Electrochim. Acta* **2007**, *52*, 6548−6553.
(49) Tench, D.; Warren, L. F. *J. Electrochem. Soc.* **1983**, *130*, 869−872.
(50) Allmand, A. J.; Campbell, A. N. *Trans. Faraday Soc.* **1924**, *19*, 559−570.
(51) Fleischmann, M.; Thirsk, H. R.; Tordesillas, I. M. *Trans. Faraday Soc.* **1962**, *58*, 1865−1877.
(52) Tang, Q.; Jiang, L.; Liu, J.; Wang, S.; Sun, G. *ACS Catal.* **2014**, *4*, 457−463.
(53) Roche, I.; Chaînet, E.; Chatenet, M.; Vondrák, J. *J. Phys. Chem. C* **2007**, *111*, 1434−1443.
(54) Pang, S. C.; Anderson, M. A.; Chapman, T. W. *J. Electrochem. Soc.* **2000**, *147*, 444−450.

DOI: 10.1021/acscatal.5b01444
ACS Catal. 2015, 5, 6021−6031

(55) Fernandes, J. B.; Desai, B. D.; Dalal, V. N. K. *J. Power Sources* **1985**, *15*, 209−237.
(56) Hansen, H. A.; Rossmeisl, J.; Norskov, J. K. *Phys. Chem. Chem. Phys.* **2008**, *10*, 3722−3730.
(57) Brock, S. L.; Duan, N.; Tian, Z. R.; Giraldo, O.; Zhou, H.; Suib, S. L. *Chem. Mater.* **1998**, *10*, 2619−2628.
(58) Kanungo, S. B.; Parida, K. M.; Sant, B. R. *Electrochim. Acta* **1981**, *26*, 1147−1156.
(59) Post, J. E. *Proc. Natl. Acad. Sci. U. S. A.* **1999**, *96*, 3447−3454.
(60) Baur, W. *Acta Crystallogr., Sect. B: Struct. Crystallogr. Cryst. Chem.* **1976**, *32*, 2200−2204.
(61) Thackeray, M. M. *Prog. Solid State Chem.* **1997**, *25*, 1−71.
(62) Cockayne, E.; Li, L. *Chem. Phys. Lett.* **2012**, *544*, 53−58.
(63) Grundy, A. N.; Hallstedt, B.; Gauckler, L. *J. Phase Equilib.* **2003**, *24*, 21−39.
(64) Fritsch, S.; Post, J. E.; Navrotsky, A. *Geochim. Cosmochim. Acta* **1997**, *61*, 2613−2616.
(65) Kohler, T.; Armbruster, T.; Libowitzky, E. *J. Solid State Chem.* **1997**, *133*, 486−500.
(66) Geller, S. *Acta Crystallogr., Sect. B: Struct. Crystallogr. Cryst. Chem.* **1971**, *27*, 821−828.
(67) Satomi, K. *J. Phys. Soc. Jpn.* **1961**, *16*, 258−265.
(68) Yuasa, M.; Yamazoe, N.; Shimanoe, K. *J. Electrochem. Soc.* **2011**, *158*, A411−A416.
(69) Hayashi, M.; Uemura, H.; Shimanoe, K.; Miura, N.; Yamazoe, N. *Electrochem. Solid-State Lett.* **1998**, *1*, 268−270.
(70) Hyodo, T.; Hayashi, M.; Miura, N.; Yamazoe, N. *J. Electrochem. Soc.* **1996**, *143*, L266−L267.
(71) Goodenough, J. B.; Manoharan, R.; Paranthaman, M. *J. Am. Chem. Soc.* **1990**, *112*, 2076−2082.
(72) Yokoi, Y.; Uchida, H. *Catal. Today* **1998**, *42*, 167−174.
(73) Harrison, W. A. *Phys. Rev. B: Condens. Matter Mater. Phys.* **2010**, *81*, 045433.
(74) Stoerzinger, K. A.; Choi, W. S.; Jeen, H.; Lee, H. N.; Shao-Horn, Y. *J. Phys. Chem. Lett.* **2015**, *6*, 487−492.
(75) Suntivich, J.; Hong, W. T.; Lee, Y.-L.; Rondinelli, J. M.; Yang, W.; Goodenough, J. B.; Dabrowski, B.; Freeland, J. W.; Shao-Horn, Y. *J. Phys. Chem. C* **2014**, *118*, 1856−1863.
(76) Alonso, J. A.; Martínez-Lope, M. J.; Casais, M. T.; Fernández-Díaz, M. T. *Inorg. Chem.* **2000**, *39*, 917−923.
(77) Kasper, N. V.; Troyanchuk, I. O. *J. Phys. Chem. Solids* **1996**, *57*, 1601−1607.
(78) Menezes, P. W.; Indra, A.; Sahraie, N. R.; Bergmann, A.; Strasser, P.; Driess, M. *ChemSusChem* **2015**, *8*, 164−171.
(79) Xu, C.; Lu, M.; Zhan, Y.; Lee, J. Y. *RSC Adv.* **2014**, *4*, 25089−25092.
(80) Cheng, F.; Shen, J.; Peng, B.; Pan, Y.; Tao, Z.; Chen, J. *Nat. Chem.* **2011**, *3*, 79−84.
(81) Cheng, F.; Zhang, T.; Zhang, Y.; Du, J.; Han, X.; Chen, J. *Angew. Chem., Int. Ed.* **2013**, *52*, 2474−2477.
(82) Cao, Y. L.; Yang, H. X.; Ai, X. P.; Xiao, L. F. *J. Electroanal. Chem.* **2003**, *557*, 127−134.
(83) Vondrak, J.; Klapste, B.; Velicka, J.; Sedlarikova, M.; Reiter, J.; Roche, I.; Chainet, E.; Fauvarque, J.; Chatenet, M. *J. New Mater. Electrochem. Syst.* **2005**, *8*, 209−212.
(84) Roche, I.; Chaînet, E.; Chatenet, M.; Vondrák, J. *J. Appl. Electrochem.* **2008**, *38*, 1195−1201.
(85) Ramaswamy, N.; Hakim, N.; Mukerjee, S. *Electrochim. Acta* **2008**, *53*, 3279−3295.
(86) Chen, C.; Levitin, G.; Hess, D. W.; Fuller, T. F. *J. Power Sources* **2007**, *169*, 288−295.
(87) Poux, T.; Bonnefont, A.; Kéranguéven, G.; Tsirlina, G. A.; Savinova, E. R. *ChemPhysChem* **2014**, *15*, 2108−2120.
(88) Poux, T.; Bonnefont, A.; Ryabova, A.; Kerangueven, G.; Tsirlina, G. A.; Savinova, E. R. *Phys. Chem. Chem. Phys.* **2014**, *16*, 13595−13600.
(89) Sunarso, J.; Torriero, A. A. J.; Zhou, W.; Howlett, P. C.; Forsyth, M. *J. Phys. Chem. C* **2012**, *116*, 5827−5834.
(90) Hancock, C. A.; Ong, A. L.; Slater, P. R.; Varcoe, J. R. *J. Mater. Chem. A* **2014**, *2*, 3047−3056.
(91) Zurilla, R. W.; Sen, R. K.; Yeager, E. *J. Electrochem. Soc.* **1978**, *125*, 1103−1109.
(92) Broughton, D. B.; Wentworth, R. L.; Laing, M. E. *J. Am. Chem. Soc.* **1947**, *69*, 744−747.
(93) Broughton, D. B.; Wentworth, R. L. *J. Am. Chem. Soc.* **1947**, *69*, 741−744.
(94) Goldstein, J. R.; Tseung, A. C. C. *J. Catal.* **1974**, *32*, 452−465.
(95) Lee, Y. N.; Lago, R. M.; Fierro, J. L. G.; González, J. *Appl. Catal., A* **2001**, *215*, 245−256.
(96) Yang, H.; Zhang, T.; Tian, H.; Tang, J.; Xu, D.; Yang, W.; Lin, L. *React. Kinet. Catal. Lett.* **2001**, *73*, 311−316.
(97) Soleymani, M.; Moheb, A.; Babakhani, D. *Chem. Eng. Technol.* **2011**, *34*, 49−55.
(98) Cremer, E. *Adv. Catal.* **1955**, *7*, 75−91.
(99) Benbow, E. M.; Kelly, S. P.; Zhao, L.; Reutenauer, J. W.; Suib, S. L. *J. Phys. Chem. C* **2011**, *115*, 22009−22017.
(100) Yuan, X.-Z.; Li, X.; Qu, W.; Ivey, D. G.; Wang, H. *ECS Trans.* **2011**, *35*, 11−20.
(101) Han, X.; Zhang, T.; Du, J.; Cheng, F.; Chen, J. *Chem. Sci.* **2013**, *4*, 368−376.
(102) Tan, Y.; Xu, C.; Chen, G.; Fang, X.; Zheng, N.; Xie, Q. *Adv. Funct. Mater.* **2012**, *22*, 4584−4591.
(103) Valim, R. B.; Santos, M. C.; Lanza, M. R. V.; Machado, S. A. S.; Lima, F. H. B.; Calegaro, M. L. *Electrochim. Acta* **2012**, *85*, 423−431.
(104) Lima, F. H. B.; Calegaro, M. L.; Ticianelli, E. A. *Electrochim. Acta* **2007**, *52*, 3732−3738.
(105) Calegaro, M. L.; Lima, F. H. B.; Ticianelli, E. A. *J. Power Sources* **2006**, *158*, 735−739.
(106) Zhu, C.; Nobuta, A.; Nakatsugawa, I.; Akiyama, T. *Int. J. Hydrogen Energy* **2013**, *38*, 13238−13248.
(107) Mao, L.; Sotomura, T.; Nakatsu, K.; Koshiba, N.; Zhang, D.; Ohsaka, T. *J. Electrochem. Soc.* **2002**, *149*, A504−A507.
(108) Matsuki, K.; Kamada, H. *Electrochim. Acta* **1986**, *31*, 13−18.
(109) Zhang, T.; Cheng, F.; Du, J.; Hu, Y.; Chen, J. *Adv. Energy Mater.* **2015**, *5*, DOI: 10.1002/aenm.201400654.
(110) Xiao, W.; Wang, D.; Lou, X. W. *J. Phys. Chem. C* **2010**, *114*, 1694−1700.
(111) Wei, C.; Yu, L.; Cui, C.; Lin, J.; Wei, C.; Mathews, N.; Huo, F.; Sritharan, T.; Xu, Z. *Chem. Commun.* **2014**, *50*, 7885−7888.
(112) Pourbaix, M. *Atlas of Electrochemical Equilibria in Aqueous Solutions*; Pergamon: Oxford, 1966; p 19.
(113) Su, H.-Y.; Gorlin, Y.; Man, I. C.; Calle-Vallejo, F.; Norskov, J. K.; Jaramillo, T. F.; Rossmeisl, J. *Phys. Chem. Chem. Phys.* **2012**, *14*, 14010−14022.
(114) Rong, X.; Kolpak, A. M. *J. Phys. Chem. Lett.* **2015**, *6*, 1785−1789.
(115) Gorlin, Y.; Lassalle-Kaiser, B.; Benck, J. D.; Gul, S.; Webb, S. M.; Yachandra, V. K.; Yano, J.; Jaramillo, T. F. *J. Am. Chem. Soc.* **2013**, *135*, 8525−8534.
(116) Chang, J.-K.; Lee, M.-T.; Tsai, W.-T. *J. Power Sources* **2007**, *166*, 590−594.
(117) Lima, F. H. B.; Calegaro, M. L.; Ticianelli, E. A. *J. Electroanal. Chem.* **2006**, *590*, 152−160.
(118) McBreen, J. *Electrochim. Acta* **1975**, *20*, 221−225.
(119) Kozawa, A.; Yeager, J. F. *J. Electrochem. Soc.* **1965**, *112*, 959−963.
(120) Navrotsky, A.; Ma, C.; Lilova, K.; Birkner, N. *Science* **2010**, *330*, 199−201.
(121) Bozzini, B.; Bocchetta, P.; Gianoncelli, A.; Mele, C.; Kiskinova, M. *ChemElectroChem* **2015**.
(122) Stoerzinger, K. A.; Hong, W. T.; Crumlin, E. J.; Bluhm, H.; Biegalski, M. D.; Shao-Horn, Y. *J. Phys. Chem. C* **2014**, *118*, 19733−19741.
(123) Hardin, W. G.; Mefford, J. T.; Slanac, D. A.; Patel, B. B.; Wang, X.; Dai, S.; Zhao, X.; Ruoff, R. S.; Johnston, K. P.; Stevenson, K. J. *Chem. Mater.* **2014**, *26*, 3368−3376.

DOI: 10.1021/acscatal.5b01444
ACS Catal. 2015, 5, 6021−6031

(124) Sun, W.; Hsu, A.; Chen, R. *J. Power Sources* **2011**, *196*, 627−635.
(125) Park, H.-Y.; Shin, T. J.; Joh, H.-I.; Jang, J. H.; Ahn, D.; Yoo, S. J. *Electrochem. Commun.* **2014**, *41*, 35−38.

DOI: 10.1021/acscatal.5b01444
ACS Catal. 2015, 5, 6021−6031